Ultra-high resolution trace element mapping provides new clues on the origin of the McArthur River (HYC) sediment-hosted Zn-Pb-Ag deposit

Sam Spinks[1,2], Mark Pearce[1], Chris Ryan[1], Gareth Moorhead[1], Robin Kirkham[1], Heather Sheldon[1], Marcus Kunzmann[1,3], Weihua Liu[1], Teagan N Blaikie[1,3], Peter Schaubs[1] and William DA Rickard[4]

Introduction

The supergiant McArthur River (Here's Your Chance [HYC]) Zn-Pb-Ag deposit is one of the largest sediment-hosted base metal deposits in the McArthur–Isa superbasin (**Figure 1**), the world's largest Zn-Pb province. HYC is widely regarded as one of the classic examples of a sedimentary exhalative (sedex) base metal deposit (Large *et al* 1998, Ireland *et al* 2004b), which implies mineralisation occurred following exhalation of a metalliferous brine into the water column with resultant deposition of laminated base metal sulfide ore as a chemical sediment. This model of ore formation influences exploration approaches as it infers a direct control of the sedimentary environment and synsedimentary tectonic framework on base metal deposition. A review of sedimentary-hosted Zn-Pb deposits by (Leach *et al* 2005) found the term 'sedex' to be fundamentally concerning because it imparts a specific

Figure 1. Simplified regional geology map of the McArthur and Mount Isa basins in northern Australia showing the locations of major stratiform Zn-Pb-Ag deposits with the McArthur River (HYC) deposit in the Batten Fault Zone highlighted.

---

[1] CSIRO Mineral Resources, Australian Resources Research Centre (ARRC), 26 Dick Perry Avenue, Kensington WA 6151, Australia

[2] Email: sam.spinks@CSIRO.au

[3] Northern Territory Geological Survey, GPO Box 4550, Darwin NT 0801, Australia

[4] John De Laeter Centre, Curtin University, Bentley WA 6102, Australia

exhalative genetic component, given most deposits lack unequivocal evidence for exhalative ore. The presence of laminated ore textures, often regarded as the primary evidence for exhalative processes in these deposits, have been shown to result from carbonate replacement processes in the subsurface well after deposition of the host sediment in other similar deposits such as in the Red Dog region (Kelley *et al* 2004). Likewise, the laminated ore of the Century deposit in the Isa basin has been shown to be ca 28 My younger than the host sediment (Broadbent *et al* 1998).

The evidence for a synsedimentary-exhalative origin of HYC (and other similar deposits in the region) is predicated mainly on the observation that the ores with fine-grained laminated textures are sedimentary in origin (Large *et al* 1998), and that ore clasts that occur within intraformational breccias indicate mineralisation occurred before individual fault movements (Ireland *et al* 2004b). Trace element enrichments, eg thallium (Tl) in the ore zone and surrounding and overlying lithologies, are also reported to represent a synsedimentary origin for mineralisation (Large *et al* 2000). These features have also been interpreted by some workers to be strong evidence for subsurface diagenetic-epigenetic carbonate replacement origin for the mineral system. Despite having been well studied over the decades, controversy remains over the genetic model of the HYC mineral system.

Herein we present evidence for a carbonate replacement-style mineral system for HYC by employing state-of-the-art analytical techniques, and, critically, by quantitatively examining the mineral system through a range of scales from the sub metre to the nanometre scale.

Methods summary

Finely laminated ore occurs in the central zone, whereas the facies in the northern and southern margins are dominated by predominantly nodular carbonate and interbedded finely-laminated pyrite (eg Ireland *et al* 2004b). Samples up to ~50 cm in diameter bearing both textures were collected from the central, southern and northern margins of the HYC pit as was exposed between 2016 and 2018.

Maia Mapper ultra-high resolution XRF mapping

The Maia Mapper is a new laboratory XRF mapping system for efficient elemental imaging of drill core sections for use in minerals research and industrial applications. It targets intermediate spatial scales, with imaging of up to ~80 M pixels, each 30 µm, over a 500 long × 150 mm high sample area, as part of the analytical workflow of the CSIRO Advanced Resource Characterisation Facility, which spans spatial scales from atomic to ore deposit scales. It brings together (i) the Maia detector and imaging system, which is part of the Australian Synchrotron XFM facility (Siddons *et al* 2014), with its capabilities for high efficiency detection (1.3 sr solid-angle), event-mode operation, millisecond pixel transit times in fly-scan mode and real-time spectral deconvolution and imaging (Ryan *et al* 2014); (ii) the high brightness MetalJet D2 liquid metal micro-focus X-ray source from Excillum (http://www.excillum.com/) with indium alloy anode and 200 W power at 70 kV into an effective 20 µm source size, filtered using a 1.0 mm aluminium window; and (iii) an efficient XOS polycapillary lens with a flux gain 15 900 at 21 keV into a ~32 µm focus; all are integrated with stage raster scanning for automated imaging and analysis of drill core sections (Ryan *et al* 2018).

Imaging for Maia Mapper uses an extension of the GeoPIXE method for synchrotron XRF analysis and imaging (Ryan *et al* 2010a), which is built on a fundamental parameters approach combined with the Dynamic Analysis method for quantitative image projection (Ryan and Jamieson 1993, Ryan 2000, Ryan *et al* 2010b). Within the approximation of constant yields across the image area, these images are quantitative and can be directly interrogated for elemental concentrations. Methods have been developed for post-imaging iterative corrections in GeoPIXE to account for the effects on yields of variations in matrix composition across the image area; these are described in detail elsewhere (Ryan 2000). Synchrotron XRF uses a monochromatic X-ray beam. For Maia Mapper, which uses a filtered microfocus XRF source spectrum, the modelling of calculated X-ray yields for each chemical element is integrated over the model filtered source spectrum.

Polished slab samples 300–400 mm in length from the central, southern and northern zones of the pit were analysed on the Maia Mapper. Particular focus was paid to the distribution of Tl, which is otherwise difficult, if not impossible, to detect as a trace element within major minerals using standard laboratory XRF techniques due to X-ray peak overlaps with Pb and S. Therefore, validation of Tl distribution requires interrogation of some spatial regions to explore and extract the Tl signal. The close proximity of Tl and Pb X-ray peaks may lead to some Tl artefact when Pb is high. Hence, we use associations to select high-Tl, but low-Pb pixels to separate each element in geochemical maps (**Figure 5**).

Electron backscatter diffraction (EBSD)

Samples were polished with a 20 nm, colloidal silica suspension in dilute NaOH to remove crystal lattice damage from thin section preparation. The surface was coated with a ~5 nm carbon coat to prevent charging in the scanning electron microscope (SEM). Electron backscatter diffraction (EBSD) mapping was performed using a Zeiss UltraPlus FEGSEM fitted with an Oxford Instruments Symmetry EBSD detector and XMaxN-80 EDS detector. During mapping, both EBSD patterns and EDS spectra were collected from each point simultaneously to allow relationships between crystallographic (grain) boundaries and chemical variations to be examined. Data was acquired using an incident electron beam with a beam current of 15 nA and accelerating voltage of 20 keV. The sample normal was inclined at 70° to the incident electron beam to increase diffracted electron yield. Maps were collected with a step size between measurements of 150 nm (to ensure that sub-micron grains were captured) and at an acquisition rate of 390 Hz. EBSD patterns were indexed against orientation databases selected by the user for the following phases: dolomite (Laue class $\bar{3}$; a = 4.807, c = 16.003), pyrite (Laue class m$\bar{3}$; a = 5.428), quartz (Laue class m$\bar{3}$; a = 4.915, c = 5.407), and sphalerite (Laue class m$\bar{3}$m; a = 5.918).

Focussed ion beam time of flight secondary ionisation mass spectrometry (FIB–TOF–SIMS)

The trace element content of pyrite was mapped at high spatial resolution using 'focussed ion beam time of flight secondary ionisation mass spectrometry' (FIB–TOF–SIMS). A focussed gallium (Ga) ion beam is used to sputter material from the surface of the sample and that material is accelerated into a time of flight mass spectrometer attached to the microscope. The resulting spectrum consists of peaks at different mass-to-charge ratios, which can be interpreted in terms of isotopes present in the sample. Plotting spatial variations in peak intensity gives a map of the relative abundance of the isotope in question. Since material is removed from the sample into the mass spectrometer, the data volume can be used to show variations in 3D. However, the maps displayed in this contribution are the signal intensity integrated over the entire depth analysed. Data were collected using a Tescan LYRA3GM FIB–SEM with a Tofwerk TOF–SIMS. Samples were coated with 10 nm of carbon to prevent charging; areas of interest were sputtered with a 69 Ga+ ion beam with an accelerating voltage 30 keV, and probe current of 300 pA using the TOF–SIMS in positive mode. Regions of interest consist of 1024 × 1024 pixels over 15 × 15 µm binned at 4 analytical pixels per display pixel to increase signal to noise ratio, which gives an effective pixel size of 58.6 nm.

Results

Paragenesis of base metal sulfides and relationship to carbonate

Large samples of laminated ore analysed on the Maia Mapper show thin laminae of base metal sulfides and pyrite as shown in the RGB element map (**Figure 2**). Discreet residual carbonate laminae are detectible in all samples analysed. For example, **Figure 2b** shows isolated calcium (Ca-blue) laminae which represent preserved carbonate (dolomite) laminae in the ore. Sphalerite (Zn-green) in these areas occurs within and around residual carbonate (**Figure 3**). In all nodular carbonate samples analysed in this study, sphalerite is spatially associated with the outer margins of carbonate (**Figure 4**). Only very minor sphalerite was detected in laminated primary (syngenetic) pyrite-organic laminae. Detailed EBSD analysis of the interfaces between sphalerite and carbonate (**Figure 5b**, **c**) shows localised Mn enrichment on the outer margins of dolomite surrounded by sphalerite, with stylolitic dissolution cavities in the carbonate hosting the majority of the sphalerite.

Thallium distribution

Interrogation of the Maia Mapper data from large HYC pit samples shows zones of high-Tl and low-Pb in some areas that seem unique spatially but not distinct in any other element image, although Fe (pyrite) is high in these zones. The sample shown in **Figure 4** hosts one such area of high-Tl within the pyritic band in the middle. By selecting this band of pixels with high-Tl, we are able to highlight the high-Tl- and low-Pb pixel associations to filter out any artefacts (overlaps) as shown in **Figure 6**. The region spectrum fit

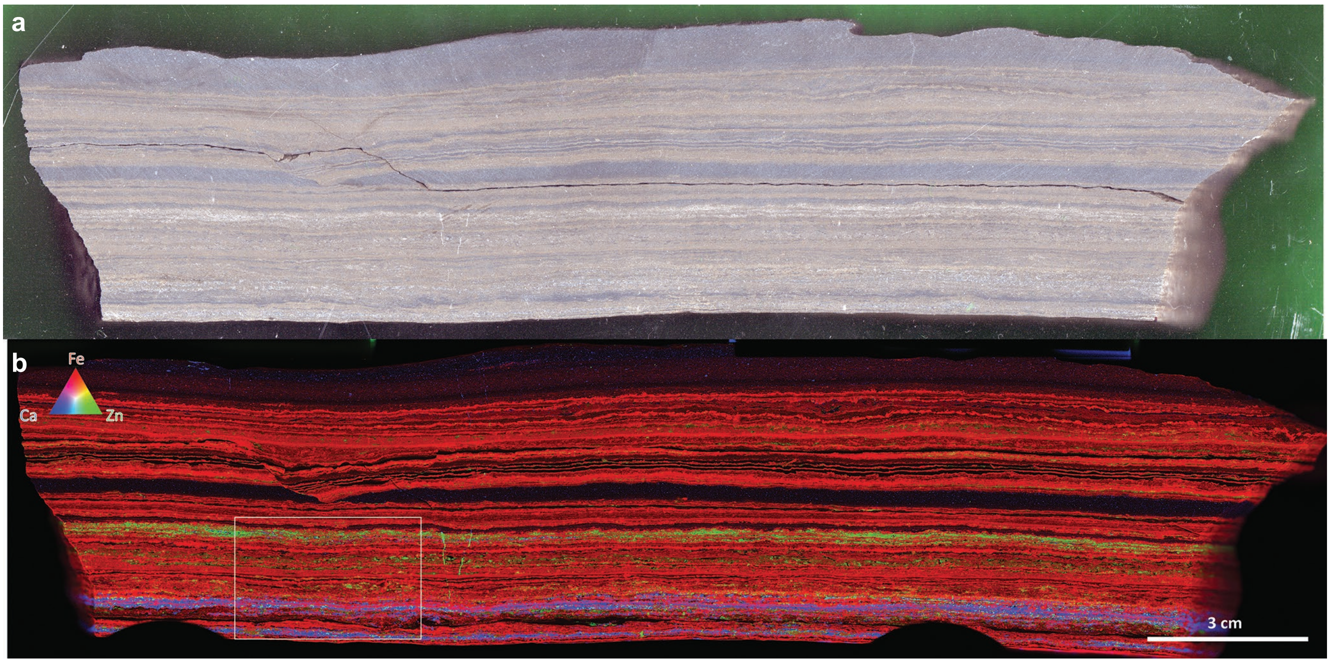

Figure 2. (**a**) Polished slab of laminated pyritic-dolomitic Zn-Pb ore (orebody 8) from central zone of HYC. (**b**) Maia Map of same sample showing distribution of iron (red), zinc (green) and calcium (blue). Zinc (sphalerite) is observed to have partially-to-fully replaced dolomitic (calcium-blue) laminae. White box indicates field of view of detailed area shown in **Figure 3**.

shows very clear Tl lines. The Tl Lα is less clear, in the side of the Pb Lα peak. But the Tl Lβ makes a good shoulder on the Pb Lβ peak, at an energy where we do not see many lines around 12.2 keV. Therefore, Tl appears genuine. This pattern is observed throughout our sample suite from HYC.

Figure 7 shows Maia Mapper data of the same slumped laminated pyrite-carbonate sample in **Figure 4**, highlighting Tl distribution. Maia Mapper analyses shows, for the first time, that high-concentration thallium is associated exclusively with pyrite. The middle

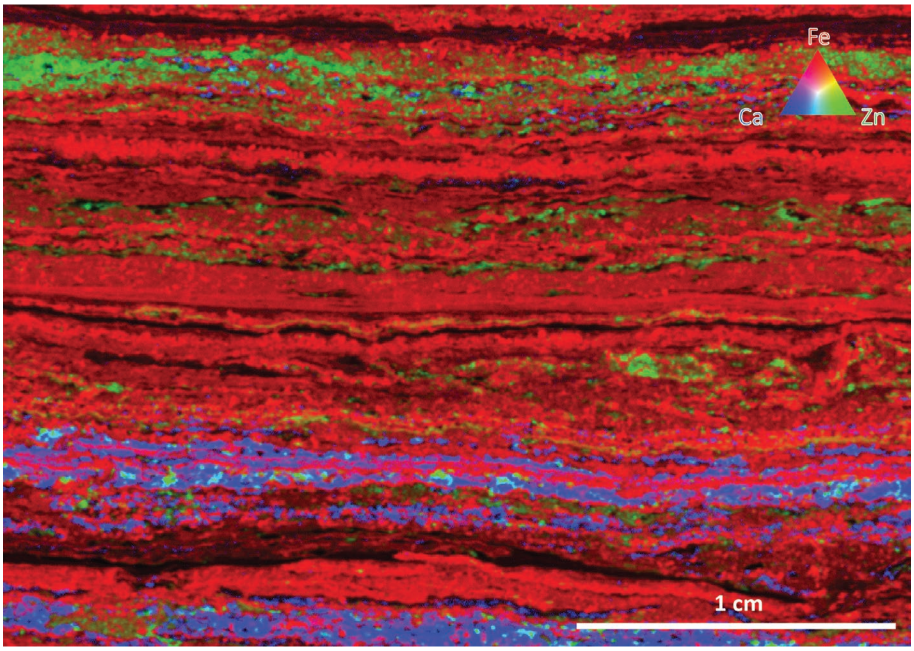

Figure 3. Maia Map of area shown by white box in **Figure 2** showing distribution of iron (red), zinc (green) and calcium (blue). Zinc (sphalerite) is observed to have partially-to-fully replaced dolomitic (calcium-blue) laminae.

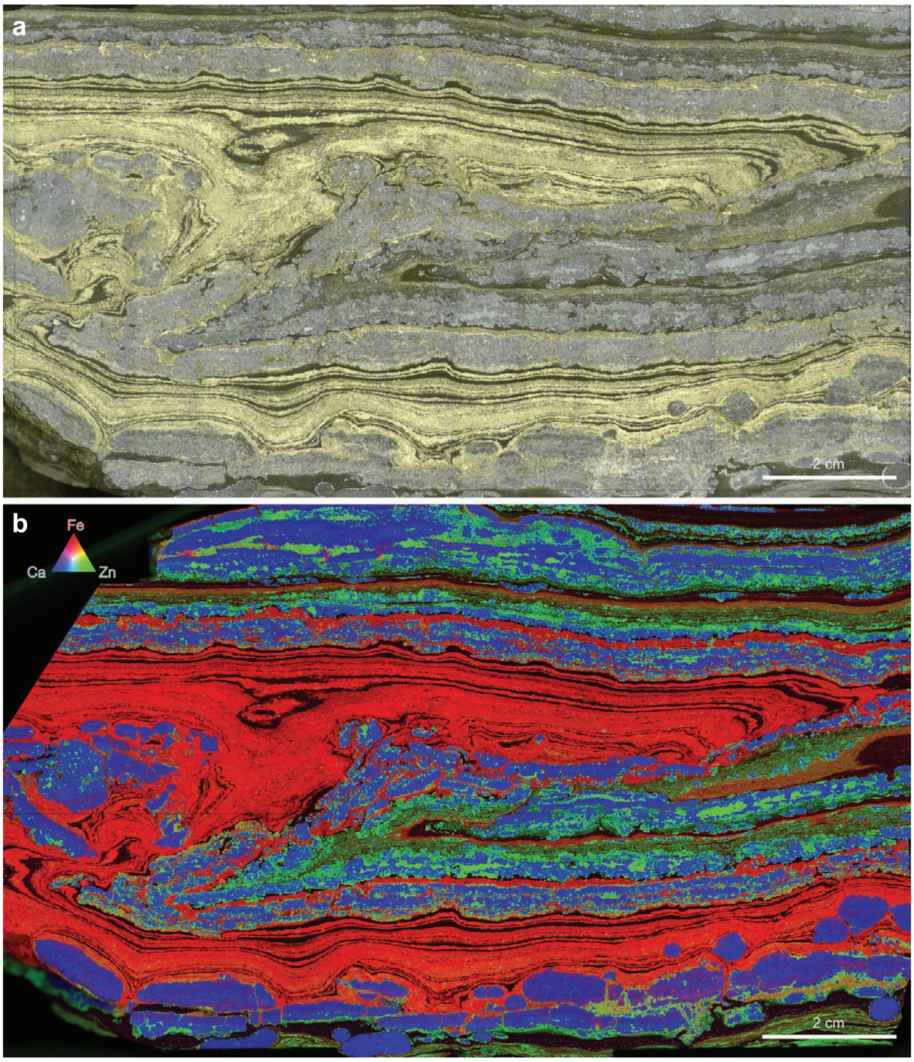

Figure 4. (**a**) Photomicrograph of polished slab of laminated and slumped pyritic and nodular carbonate Zn-Pb ore from southern margin zone of HYC. (**b**) Maia Map of same sample showing distribution of iron (red), zinc (green) and calcium (blue).

image shows Tl (red), which when compared with the photomicrograph of the sample above, demonstrates that the highest concentrations (brightest colours) correlate with paragenetically-late pyrite bands that are spatially proximal to the sphalerite (Zn - blue) occurring around the rims of nodular carbonate, also shown in **Figure 4b**. Thallium enrichment also occurs in early syngenetic laminated pyrite zones but in lower concentrations. However, galena (Pb - green), which occurs in association with certain carbonate nodule margins, is not spatially-associated with Tl enrichment in the late pyritic bands. **Figure 7c** shows the high-Tl low-Pb pixels highlighted as a distribution heat map. This image clearly shows the Tl concentration variation between the zone of syngenetic laminated pyrite and the bands of later diagenetic pyrite (up to ~811 ppm). This image also shows zones of probable X-ray artefact (overlap) with Pb in the upper and lower areas where Pb concentrations are high (**Figure 7b**).

Closer SEM analysis of the zones of Tl-enriched late pyrite (eg **Figure 7**) shows the pyrites bear rounded (possibly framboidal) cores with numerous generations of later euhedral overgrowths (**Figure 8a**). Pyrite overgrowths contain minor galena inclusions. Sphalerite that is observed replacing carbonate (dolomite) throughout, is here observed to have entirely precipitated after the latest pyrite overgrowths. Detailed analysis of these overgrown

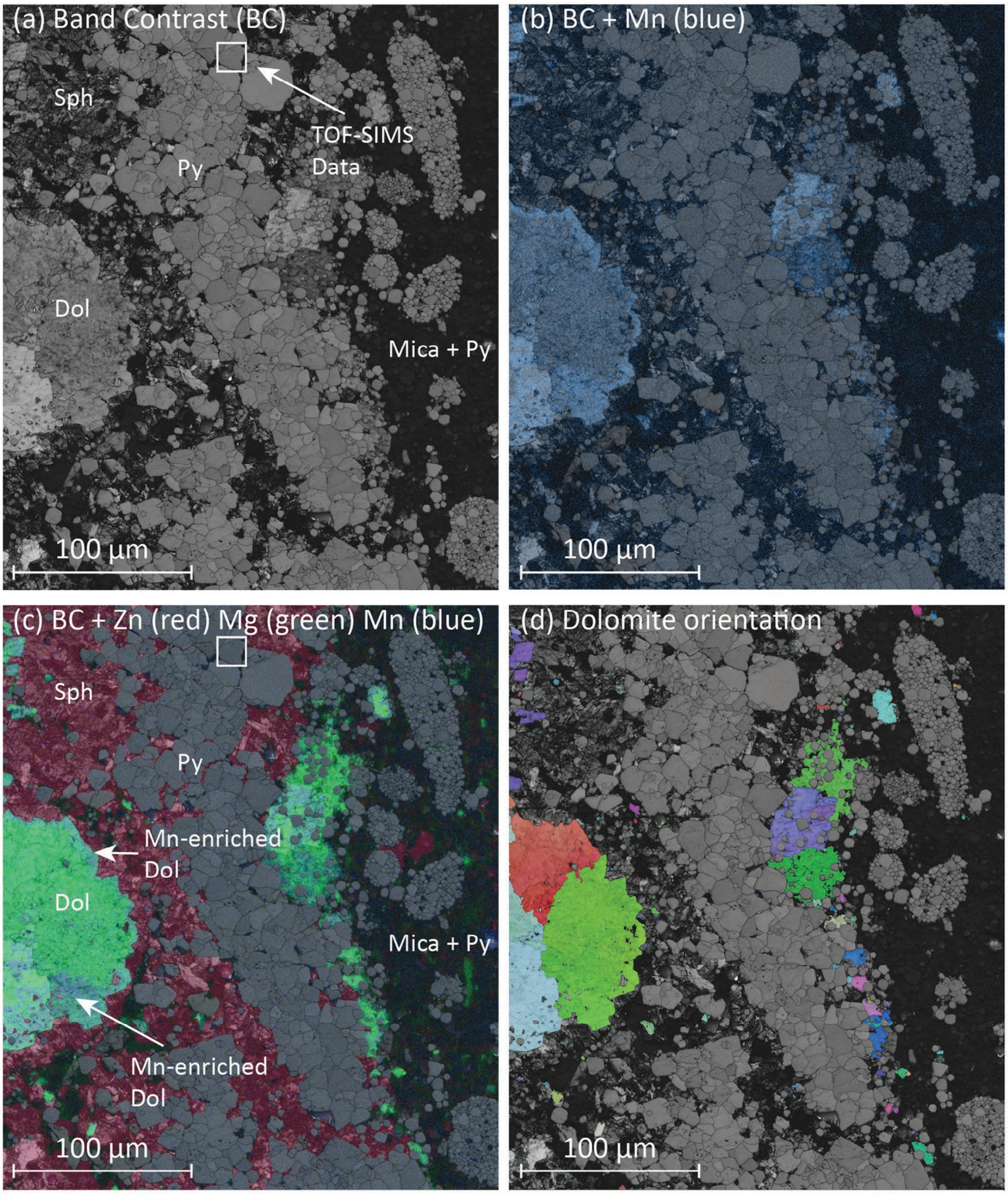

Figure 5. EBSD montage of pyritic-sphalerite-dolomite in approximate area shown in white box in **Figure 7c**. EBSD–EDS data is presented as maps combining different components of the data to show spatial relationships. (**a**) Band contrast, a measure of EBSD pattern quality, is used as a background image because it displays the microstructure complete with grain boundaries. (**b**) Overlaying Mn intensity from the EDS data shows that Mn largely resides in dolomite (cf **Figures 5b**, **d**) adjacent to phase boundaries between dolomite and sphalerite (the latter shown by the presence of Zn in **Figure 5c**. (**c**) BC+Zn (red) Mg (green) Mn (blue). (**d**) Dolomite orientation. BC=band contrast; Dol=dolomite; Sph=sphalerite; Py=pyrite.

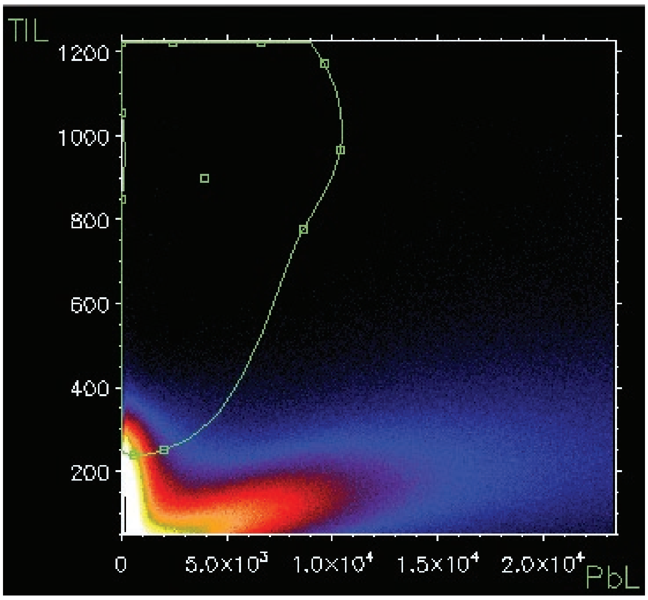

Figure 6. Comparison of thallium Lα and lead Lα regions in area outlined by white box in thallium-rich zone, shown in **Figure 7c**.

framboidal pyrites using FIB–TOF–SIMS shows that the distribution of Tl is concentrated in the diagenetic overgrowths (**Figure 8b**). The framboidal cores are mostly entirely void of detectable Tl (**Figure 9**), although in rare cases are there localised enrichments (eg **Figure 8b**).

Discussion

Carbonate replacement by Zn-Pb sulfides at HYC

The presence of laminated base metal sulfide textures is the primary observation historically presented as evidence for a syndepositional origin of the HYC and other deposits in the McArthur–Isa Zn belt (Ireland *et al* 2004b, Large *et al* 2000, Large *et al* 2005). The argument by Leach *et al* (2010) that sulfide layering, by itself, is not sufficient evidence for exhalative ore was recently disputed by Sangster (2018) who stated that sulfides mimicking synsedimentary textures is not proof of replacement processes either. Whilst this counter argument is valid, it emphasises the circular pattern of opposing arguments that arise when dealing with interpretations based on subjective, sometimes non-quantifiable observations. Sangster (2018) also noted that even though carbonate replacement is frequently mentioned in literature to be responsible for layered sulfide textures at HYC and elsewhere, the replaced mineral phase is ‘seldom identified’. This highlights the difficulty in visually identifying certain residual mineral phases in altered laminated sedimentary rocks; it also reflects a problem that arises from scale. Most studies are based on thin sections that are chosen on subjective, visual observational criteria at the sampling stage. Thus, traditionally there is a significant step in scale of study, from the deposit scale to thin section scale, that can lead to subtle, but potentially key features (such as residual carbonate) being overlooked. Clearly this is dictated by a historic lack of technologies capable of quantitative petrographic analyses on large samples. New technological developments such as the Maia Mapper (Ryan *et al* 2014) can not only accommodate this gap in scale, allowing data-led decision making when choosing thin sections, but also can allow trace quantitative element mapping (eg Tl) at unprecedented ultra-high resolution.

Our data (from large pit samples up to ~300 mm long) clearly demonstrate that residual laminated carbonate is locally preserved in laminated base metal sulfide ore from the central zone of HYC (**Figure 2**, **Figure 3**). Critically, when visually inspecting these samples, residual preserved sub-1 mm laminated carbonate is extremely difficult to identify. Upon closer inspection, the textures of base metal sulfide proximal to preserved carbonate in these laminated ores are consistent with carbonate dissolution. The textures in nodular carbonate-bearing ore are more readily identifiable visually but are far clearer when Maia Mapper data is examined (eg **Figure 4**).

Whilst the presence of Mn within euhedral overgrowths at the margin of dolomite aggregates is not diagnostic of replacement processes, the patchy nature of the Mn enrichment elsewhere suggests that the initially Mn-poor dolomite has been replaced at a later stage. The spatial coincidence of Mn and sphalerite is consistent with dolomite replacement during Zn mineralisation.

Thallium hosted in late diagenetic pyrite

Thallium is a highly incompatible (and toxic) trace element that is often associated with K-bearing mineral phases due to its primary Tl^+ form, which is similar in size to the monovalent cations K^+, Rb^+ and Cs^+ (Nielsen *et al* 2013). As such Tl is readily adsorbed onto clay mineral phases and Mn oxides (Martin *et al* 2018). Unlike other alkali metals, Tl has been suggested to exhibit chalcophile behaviour in hydrothermal fluids and sulfur-bearing melts (McGoldrick *et al* 1979). However, the behaviour of Tl in mineral systems is poorly understood.

Thallium enrichments have been known at HYC (Large *et al* 2000) and among numerous other similar ore deposits worldwide for decades. Previous studies have demonstrated that Tl is present in individual pyrite crystals in the HYC ore zone. Large variations in Tl concentrations in various pyrites, ranging from 176–919 ppm, were reported from the HYC ore zone by Mukherjee and Large (2017). Whilst these analyses are useful, what is critically lacking is context at a scale greater than that of a single pyrite grain. Thus, little is hitherto known about the overall deportment of Tl in the ore zone or the metallogeny of Tl in the greater HYC mineral system. Therefore, the potential of Tl as a pathfinder element in exploration for sediment-hosted Zn deposits, and in other geochemical exploration, is currently unclear.

By using new ultra-high resolution Maia Mapper technology on large-scale ore samples, our data show that Tl is detectable in both early laminated pyrite and in late diagenetic pyrite bands, but is highly concentrated in the latter phase (**Figure 7**). However, by spatially mapping the distribution of highest concentrations of Tl in late pyrite, our detailed quantitative nm-scale mapping using FIB–TOF–SIMS makes it clear that Tl is almost entirely present within diagenetic pyrite overgrowths (**Figure 8**). Furthermore, consistent with the observations of Broadbent *et al* (1998), Eldridge *et al* (1993), and Polito *et al* (2006), our data show that base metal sulfide mineralisation occurred after the latest diagenetic pyrite. Whilst this not only precludes syndepositional base metal mineralisation, we argue that there are implications for the timing of Tl enrichment in the HYC mineral system, which occurred prior to the deposition of base metal sulfides.

Fluid modelling

Thallium deportment in late pyrite suggests both Fe and Tl were transported in the same hydrothermal fluids, particularly given the homogeneity observed in the distribution within the overgrowths. Fluid phase modelling, assuming a temperature of ~150°C and a salinity of 15% eq NaCl (Cooke *et al* 2000), shows that TlCl is mobile across a range of pH values above a Log fO_2 (aq) of ~45, with S

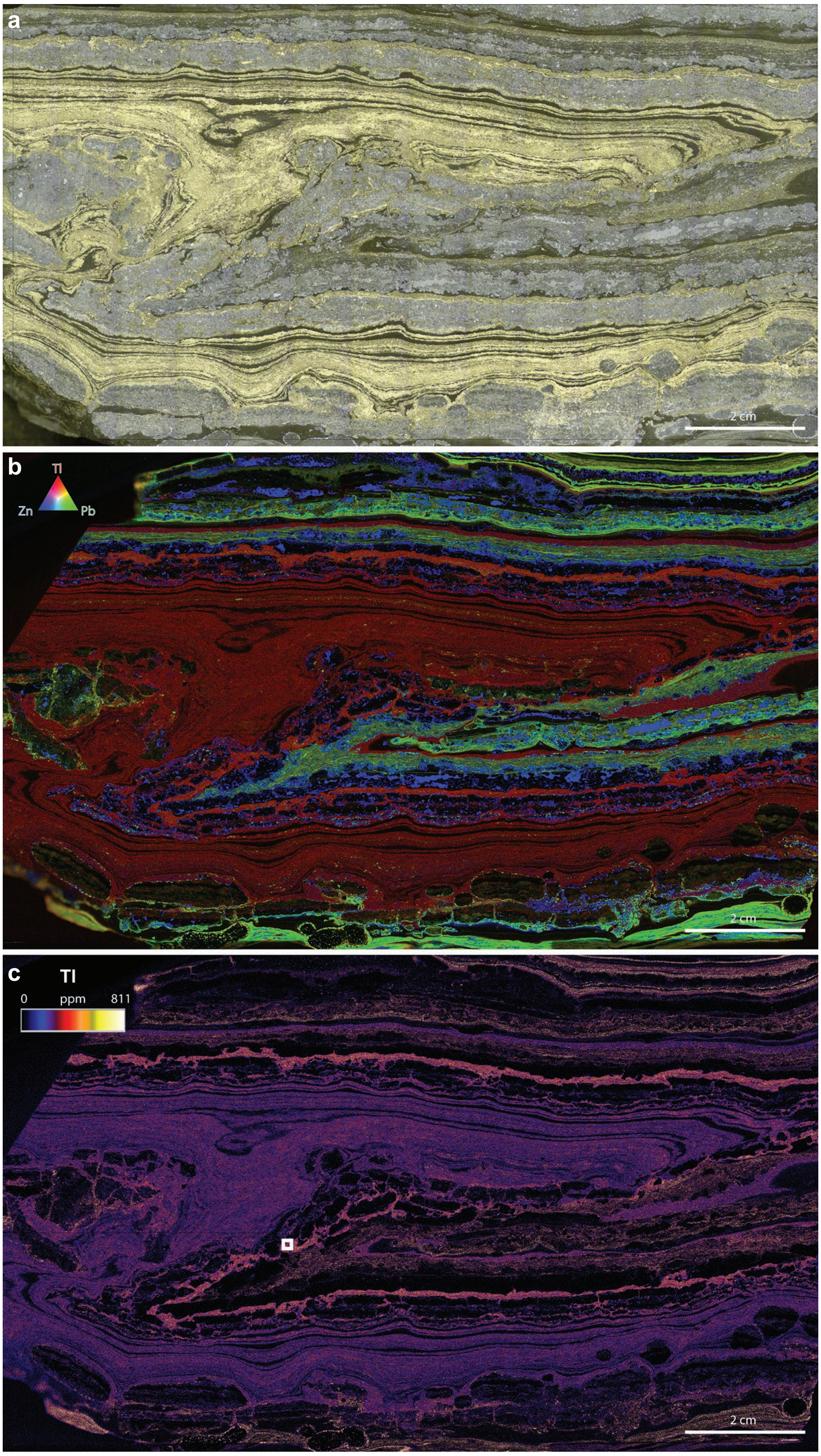

Figure 7. (**a**) Photomicrograph of polished slab of laminated pyritic-carbonate HYC Zn-Pb ore. (**b**) Maia Map of same sample showing distribution of thallium (red), zinc (green) and lead (blue). (**c**) Heat distribution map of thallium showing highest enrichments in late-stage pyrite zone. White box indicates area analysed in **Figure 5** and **Figure 6**, and approximate area of detailed TOF–SIMS analysis shown in **Figure 8**.

species buffered between pH 3–4 (**Figure 10a**). However FeCl complexes are only mobile at the same temperatures below pH 4; below Log fO_2 (aq) 45 (reducing conditions), H_2S is stable. Cooke *et al* (2000) noted the likely dominance of oxidised fluids in the Australian Proterozoic sediment-hosted Zn deposits. Our data are consistent with this; therefore, we argue that it is likely that FeCl and TlCl complexes were transported in oxidised fluids with pH below 4 (**Figure 10a**, **b**) in the presence of HSO_4^-, before being reduced thus allowing hydrothermally-derived pyrite overgrowths to precipitate.

Zinc can be transported at similar temperatures as $ZnCl_4^{2-}$ complexes across a range of pH values (0 – ~9) in oxidised fluids. Sphalerite cannot precipitate at those temperatures at pH values below ~5; therefore, pyrite and sphalerite are unlikely to have co-precipitated if the initial ore fluid was pH <4, ie transporting FeCl complexes (**Figure 10c**). Carbonate dissolution during acidic fluid influx may have created additional porosity along bedding planes. Sphalerite may have been deposited if the ore-bearing fluids were buffered to pH values >5 following acidic dissolution of carbonate, allowing reduction of the residual Zn-bearing fluid and

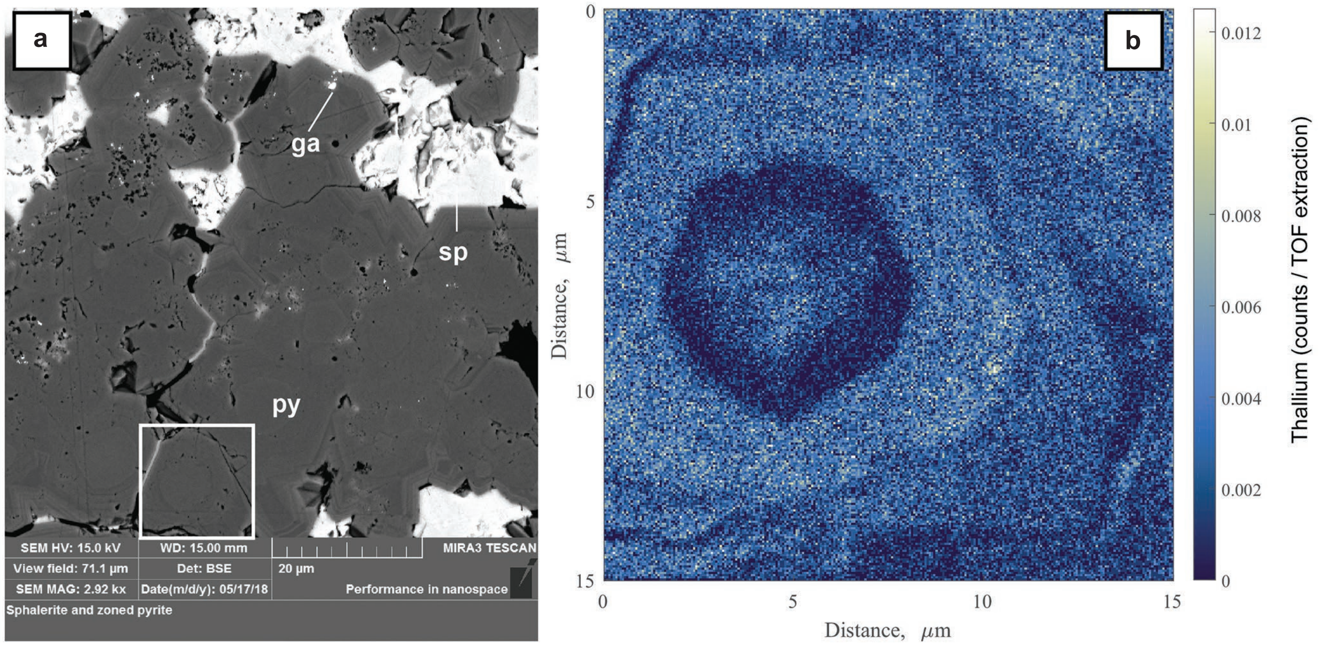

Figure 8. (**a**) SEM image of early framboidal pyrite with late zoned pyrite overgrowths in the Zn-Pb ore zone outlined in **Figure 7**. (**b**) TOF–SIMS map of Tl^{205} in zoned pyrite outlined in the white box in **8a**. The framboidal core, in this case, has rare localised enrichments in Tl, whereas the zoned overgrowths have higher Tl concentrations.

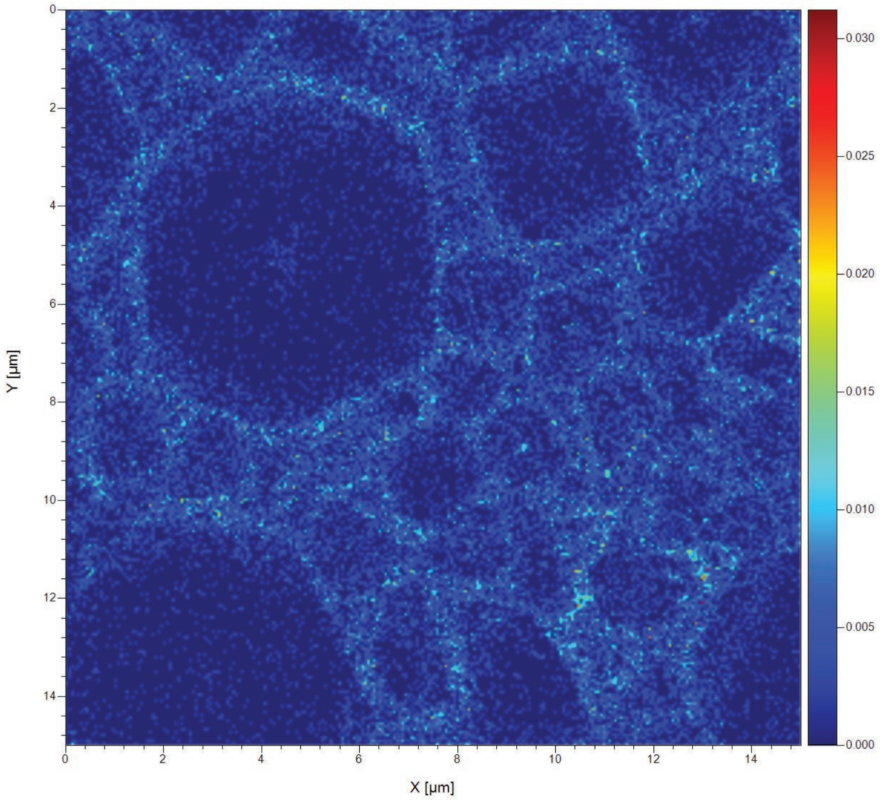

Figure 9. FIB–TOF–SIMS Tl image of framboidal pyrite cores with minimal diagenetic overgrowths, but with localised Tl enrichments on outer edge.

precipitation of sphalerite. This mechanism could explain the presence of base metal sulfides that surround latest-stage pyrite overgrowths (**Figure 8a**); this is consistent with the prior observations of Broadbent *et al* (1998), Eldridge *et al* (1993), and Polito *et al* (2006). Furthermore, as carbonates have retrograde solubilities, solubility products of Fe-Mn carbonates are lower than those of Ca-Mg-rich carbonates such that the Fe–Mn carbonates may precipitate close to the site of dissolution (Chen *et al* 2003). This is consistent with the Mn-enriched rims observed at the dissolution front observed in contact with sphalerite in **Figure 5c**.

Implications for the origin of the HYC mineral system

In the context of previous work conducted at HYC and elsewhere in the McArthur–Isa superbasin, these findings provide new quantitative insights into the genesis of sediment-hosted Zn-Pb deposits such as HYC. **Table 1** lists a summary of observations at HYC that are considered evidence for both a syndepositional-syngenetic model and a diagenetic-epigenetic model by previous studies. The summary of findings of this study in relation to each of these previous observations are also shown.

Conclusions

- Ultra-high resolution geochemical mapping of large pit samples from HYC show sphalerite is exclusively associated with carbonate dissolution. Nodular carbonate in north and south zones is partially-replaced, whereas laminated carbonate in the central zone is almost entirely replaced by base metal sulfides.
- EBSD analyses show Mn-enriched outer margins of carbonate at dissolution front in contact with sphalerite.
- Ultra-high resolution geochemical mapping shows Tl is hosted in late-stage pyrite bands, spatially associated with sphalerite. FIB–TOF–SIMS analyses shows Tl is hosted predominantly in late-stage pyrite overgrowths that precipitated (perhaps immediately) before base metal sulfides.
- Fluid modelling suggests precipitation of initial Tl-bearing pyrite overgrowths by reduction of metals transported by acidic (pH<4) oxidised fluids. Acidic dissolution of carbonate allows additional porosity and creates a pH buffering effect, raising fluid pH above 5, allowing precipitation of sphalerite at site of carbonate dissolution.
- These findings provide strong evidence for a diagenetic-epigenetic carbonate replacement origin for the HYC mineral system; they preclude a syngenetic model. This has implications for future exploration strategies for these Proterozoic sediment-hosted base metal deposits.

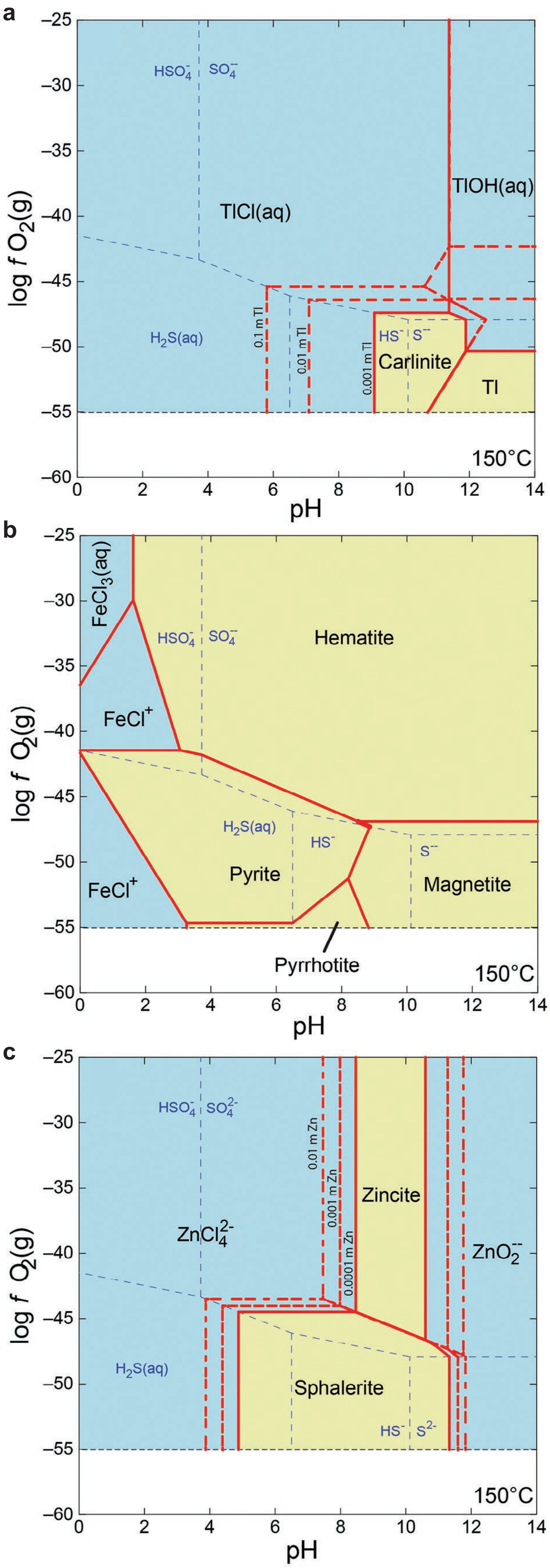

Figure 10. Stability of predominant Tl, Fe and Zn minerals and aqueous species as a function of logfO_2 and pH at 150°C: (**a**) Tl; (**b**) Fe; (**c**) Zn. Boundaries of Tl, Fe and Zn species are shown as red solid, dashed and dash-dotted lines respectively. The boundaries of sulfur species are shown with blue dashed lines in all subplots; activities of total sulfur and chloride are the same as Cooke *et al* (2000): a_∑S = 0.001 m; a_∑Cl = 5.8 m.

Table 1. Summarised constraints on the contrasting syndepositional-exhalative versus diagenetic-epigenetic genetic models based on key lines of evidence and observations. Summarised after Huston *et al* (2006).

Observation	**Syndepositional-exhalative model**	**Diagenetic-epigenetic model**	**This study**
Laminated ore textures (in central zone of deposit)	Consistent with deposition of sulfides as chemical sediments from water column (Ireland *et al* 2004b, Large *et al* 1998, Large *et al* 2005)	Can be produced by sulfide replacement of layered-laminated sedimentary sedimentary-diagenetic carbonate (Broadbent *et al* 1998, Eldridge *et al* 1993, Polito *et al* 2006) (**Figure 2**, **Figure 3**). Nodular carbonate also replaced by sphalerite (Ireland *et al* 2004b, Large *et al* 2005) (**Figure 4**, **Figure 5**).	Textures observed in this study show that both laminated and nodular carbonate were subject to partial to full dissolution and replacement by base metal sulfides. EBSD analyses of carbonate (dolomite) show that the outer edges are Mn-altered where in contact with replacive sphalerite.
Laminated ore clasts within intraformational breccias	Consistent with early syndepositional mineralisation prior to breccia flows (Ireland *et al* 2004a)	Can be produced by the same carbonate replacement geochemical processes as the main orebody, well after deposition.	Can be produced by the same carbonate replacement geochemical processes as the main orebody, well after deposition.
Timing of sphalerite and galena mineralisation (post-latest diagenetic pyrite overgrowths)	Not consistent.	Deposition of base metal sulfides after latest diagenetic pyrite overgrowths (**Figure 8**) indicate diagenetic-epigenetic model (Broadbent *et al* 1998, Eldridge *et al* 1993, Huston *et al* 2006, Leach *et al* 2010, Polito *et al* 2006).	Sphalerite and galena mineralisation occur after the latest pyrite overgrowths, with some minor galena occurring as micron-scale inclusions in some pyrite overgrowths. Fluid modelling demonstrates that initial acidic, oxidized ore fluids may have transported metal chloride complexes, followed by reduction, allowing precipitation of Tl-enriched pyrite overgrowths. Carbonate dissolution could have pH buffered the fluid to pH>5, allowing later precipitation of sphalerite.
Thallium (Tl) lithogeochemical anomalism (100s ppm)	Enrichment of Tl up to 200 m above ore zone could result from low-T fluid after main-stage mineralisation (Large *et al* 2000).	Enrichment of Tl up to 200 m above ore zone *indicate* fluid flow well after deposition of ore-hosting sediments low-T fluid after main-stage mineralisation (Huston *et al* 2006) (**Figure 7–9**)	Ultra-high resolution mapping of large samples show Tl enrichments are hosted in late-stage pyrite bands, proximal to sphalerite deposition associated with carbonate replacement. Nanometre-scale quantitative analyses show that Tl is hosted in late-stage pyrite overgrowths that precipitated before base metal sulfides. Fluid modelling shows sphalerite may have precipitated immediately after Tl-enriched pyrite overgrowths due to pH buffering following carbonate dissolution. Enrichment in Tl up to 200 m above ore zone (Large *et al* 2000), by this mechanism, would confirm fluid flow well after deposition of ore-hosting sediments.

Acknowledgements

The authors would like to thank McArthur River Mining, particularly Kris Masterman, for excellent support on site at HYC. This project is funded by the NTGS–CSIRO collaborative project on the McArthur Basin.

References

Broadbent GC, Meyers RE and Wright JV, 1998. Geology and origin of shale-hosted Zn-Pb-Ag mineralization at the Century deposit, Northwest Queensland, Australia. *Economic Geology* 93, 1264–1294.

Chen J, Walter MR, Logan GA, Hinman MC and Summons RE, 2003. The Paleoproterozoic McArthur River (HYC) Pb/Zn/Ag deposit of northern Australia: organic geochemistry and ore genesis. *Earth and Planetary Science Letters* 210, 467–479.

Cooke DR, Bull SW, Large EE and McGoldrick PJ, 2000. The importance of oxidized brines for the formation of Australian Proterozoic stratiform sediment-hosted Pb-Zn (sedex) deposits. *Economic Geology* 95, 1–18.

Eldridge CS, Williams N and Walshe JL, 1993. Sulfur isotope variability in sediment-hosted massive sulfide deposits as determined using the ion microprobe SHRIMP: II. A study of the H.Y.C. deposit at McArthur River, Northern Territory, Australia. *Economic Geology* 88, 1–26.

Huston DL, Stevens B, Southgate PN, Muhling P and Wyborn L, 2006. Australian Zn-Pb-Ag ore-forming systems: A review and analysis. *Economic Geology* 101, 1117–1157.

Ireland T, Bull SW and Large RR, 2004a. Mass flow sedimentology within the HYC Zn-Pb-Ag deposit, Northern Territory, Australia: Evidence for syn-sedimentary ore genesis. *Mineralium Deposita* 39, 143–158.

Ireland T, Large RR, McGoldrick PJ and Blake M, 2004b. Spatial distribution patterns of sulfur isotopes, nodular carbonate, and ore textures in the McArthur River (HYC) Zn-Pb-Ag deposit, Northern Territory, Australia. *Economic Geology* 99, 1687–1709.

Kelly KD, Dumoulin JA and Jennings S 2004. The Anarraaq Zn-Pb-Ag and barite deposit, northern Alaska: Evidence for replacement of carbonate by barite and sulfides. *Economic Geology* 99, 1577–1591.

Large RR, Bull SW, Cooke DR and McGoldrick PJ, 1998. A genetic model for the HYC deposit, Australia: Based on regional sedimentology, geochemistry, and sulfide-sediment relationships. *Economic Geology* 93, 1345–1368.

Large RR, Bull SW and McGoldrick PJ, 2000. Lithogeochemical halos and geochemical vectors to stratiform sediment hosted Zn-Pb-Ag deposits Part 2. HYC deposit, McArthur river, North Territory. *Journal of Geochemical Exploration* 68, 105–126.

Large RR, Bull SW, McGoldrick PJ and Walters S, 2005. Stratiform and strata-bound Zn-Pb-Ag deposits in Proterozoic sedimentary basins, northern Australia. *Economic Geology* 100, 931–963.

Leach DL, Bradley DC, Huston D, Pisarevsky SA, Taylor RD and Gardoll SJ, 2010. Sediment-hosted lead-zinc deposits in earth history. *Economic Geology* 105, 593–625.

Leach DL, Sangster DF, Kelly KD, Large RR, Garven G and Allen CR, 2005. Sediment-hosted Pb-Zn deposits: A global perspective. *Economic Geology* 100, 561–608.

Martin LA, Wissocq A, Benedetti MF and Latrille C, 2018. Thallium (Tl) sorption onto illite and smectite: Implications for Tl mobility in the environment. *Geochimica et Cosmochimica Acta* 230, 1–16.

McGoldrick PJ, Keays RR and Scott BB, 1979. Thallium: a sensitive indicator of rock/seawater interaction and of sulfur saturation of silicate melts. *Geochimica et Cosmochimica Acta* 43, 1303–1311.

Mukherjee I and Large R, 2017. Application of pyrite trace element chemistry to exploration for SEDEX style Zn-Pb deposits: McArthur Basin, Northern Territory. *Australia. Ore Geology Reviews* 81, 1249–1270.

Nielsen SG, Wasylenki LE, Rehkamper M, Peacock CL, Xus Z and Moon EM, 2013. Towards an understanding of thallium isotope fractionation during adsorption to manganese oxides. *Geochimica et Cosmochimica Acta* 117, 252–265.

Polito PA, Kyser TK, Golding SD and Southgate PN, 2006. Zinc deposits and related mineralization of the Burketown mineral field, including the world-class century deposit, northern Australia: Fluid inclusion and stable isotope evidence for basin fluid sources. *Economic Geology* 101, 1251–1273.

Ryan CG, 2000. Quantitative trace element imaging using PIXE and the nuclear microprobe. *International Journal of Imaging Systems and Technology* 11, 219–230.

Ryan CG and Jamieson DN, 1993. Dynamic analysis: on-line quantitative PIXE microanalysis and its use in overlap-resolved elemental mapping. *Nuclear Instruments and Methods in Physics Research* B77, 203–214.

Ryan CG, Kirkham R, Hough RM, Moorhead G, Siddons DP, De Jonge MD, Paterson DJ, De Geronimo G, Howarde DL and Cleverley JS, 2010a. Elemental X-ray imaging using the Maia detector array: The benefits and challenges of large solid-angle. *Nuclear Instruments and Methods in Physics Research, Section A: Accelerators, Spectrometers, Detectors and Associated Equipment* 619, 37–43.

Ryan CG, Kirkham R, Moorhead GF, Parry D, Jensen M, Faulks A, Hogan S, Dunn PA, Dodanwela R, Fisher LA, Pearce M, Siddons DP, Kuczewski A, Lundstrom U, Trolliet A and Gao N, 2018. Maia Mapper: High definition XRF imaging in the lab. *Journal of Instrumentation* 13.

Ryan CG, Siddons DP, Kirkham R, Dunn PA, Kuczewski A, Moorhead G, De Geronimo G, Paterson DJ, De Jonge MD, Hough RM, Lintern MJ, Howard DL, Kappen P and Cleverley J, 2010b. The new Maia detector system: Methods for high definition trace element imaging of natural material. *AIP Conference Proceedings* 1221, 9–17.

Ryan CG, Siddons DP, Kirkham R, Li ZY, De Jonge MD, Paterson DJ, Kuczewski A, Howard DL, Dunn PA, Falkenberg G, Boesenberg U, De Geronimo G, Fisher LA, Halfpenny A, Lintern MJ, Lombi E, Dyl KA, Jensen M, Moorhead GF, Cleverley JS, Hough RM, Godel B, Barnes SJ, James SA, Spiers KM, Alfeld M, Wellenreuther G, Vukmanovic A and Borg S, 2014. Maia X-ray fluorescence imaging: Capturing detail in complex natural samples. *Journal of Physics: Conference Series* 499, 012002.

Sangster DF 2018. Toward an integrated genetic model for vent-distal SEDEX deposits. *Mineralium Deposita* 53, 509–527.

Siddons DP, Kirkham R, Ryan CG, De Geronimo G, Dragone A, Kuczewski AJ, Li ZY, Carini GA, Pinelli D, Beuttenmuller R, Elliot D, Pfeffer M, Tyson TA, Moorhead GF and Dunn PA, 2014. Maia X-ray microprobe detector array system. *Journal of Physics: Conference Series* 499, 012001.